Colossal magnetoresistance and anisotropic spin dynamics in the antiferromagnetic semiconductor $Eu_5Sn_2As_6$

R. P. Day,[1,*] K. Yamakawa,[1,*] L. Pritchard Cairns,[1] J. Singleton,[2] W. L. Cao,[3] C. Wu,[3] M. Allen,[3] J. E. Moore,[1] and James G. Analytis[1,4,5,†]
[1]*Department of Physics, University of California, Berkeley, California 94720, USA*
[2]*Los Alamos National High Magnetic Field Lab, Los Alamos, New Mexico 87545, USA*
[3]*Department of Physics, University of California, San Diego, California 92093, USA*
[4]*CIFAR Quantum Materials, CIFAR, Ontario, Toronto M5G 1M1, Canada*
[5]*Kavli Energy NanoScience Institute, Berkeley, California 94720, USA*

(Received 11 July 2024; revised 20 November 2024; accepted 2 December 2024; published 3 February 2025)

We report on the thermodynamic and transport properties of the rare-earth Zintl compound $Eu_5Sn_2As_6$, which orders as a canted antiferromagnetic semiconductor at 10.3 K. The system also displays a complex cascade of magnetic phases arising from geometric and magnetic exchange frustration, with high sensitivity to the application and direction of small magnetic fields. At low temperature, $Eu_5Sn_2As_6$ exhibits negative colossal magnetoresistance of up to a factor of 6000. This represents a lower bound as the conductivity appears to be shunted by an unknown conduction channel, causing the resistivity to saturate. Mechanisms for the low-temperature saturation of resistivity are discussed.

DOI: 10.1103/PhysRevB.111.054406

I. INTRODUCTION

Magnetic semiconductors present a unique opportunity to explore the interplay of disparate energy scales, giving rise to a diversity of electronic and magnetic phenomena [1]. The rare-earth Zintl compounds are of particular interest, incorporating local-moment magnetism, low carrier densities, narrow band gaps, and dimensional confinement of both itinerant carriers and local moments. This combination is believed to give rise to magnetic topological insulators [2,3], exceptional thermoelectric material properties [4,5], Kondo lattice physics [6], and unconventional superconductivity [7], among others.

The quasi-one-dimensional $Eu_5Sn_2As_6$ is one such example of the rare-earth Zintl semiconductors, belonging to a structural family that include antiferromagnetic topological insulators [2,3]. In this work, we explore the low-temperature electrical and magnetic properties of this system. We observe a hierarchy of orders as a function of temperature and magnetic field, operating across distinct length and energy scales. Beginning at temperatures well above that of long-range order, magnetic clusters begin to form, binding to the dilute free carriers in the system and consistent with the formation of magnetic polarons. As temperature is reduced, this gives way to a cascade of metamagnetic transitions, as well as glassy dynamics in very low field. The interplay of these various phases within the local Eu^{2+} ions and $SnAs_3$ chains is manifest in the form of colossal magnetoresistance spanning nearly four decades, reflecting the significant exchange interaction between local moments and itinerant carriers in this low-carrier density system. Finally, at low fields and temperatures, resistance appears to shunt across a low-impedance path.

II. EXPERIMENTAL RESULTS

$Eu_5Sn_2As_6$ crystallizes in the orthorhombic space group *Pbam* (No. 55), shown schematically in Fig. 1(a). First synthesized as a candidate thermoelectric [4,8], the structure can be described as composed of one-dimensional chains of corner-sharing Sn-As tetrahedra bound together by staggered plaquettes of Eu^{2+} ions. Single crystals were prepared by a flux method. Europium metal (6N, Ames Lab) was cut up and combined with Arsenic pieces (4N, Alfa Aesar) and Tin shot (5N, Sigma Aldrich) in a 1:3:16 molar ratio in an alumina crucible under a dry nitrogen atmosphere. The crucible was sealed in an evacuated quartz ampoule without being exposed to air. The ampoule was heated in a furnace to 400 °C over 2 hours, held for 1 hour, then heated to 650 °C over 3 hours, held for 2 hours, then ramped to 1000 °C over 10 hours before holding at 1000 °C for 12 hours. Finally, the ampoule was slowly cooled to 750 °C at 2 °C/hour, and spun in a centrifuge to remove excess tin flux. This process yields long bar-shaped crystals as illustrated in Fig. 1(b) with a typical length of 3–10 mm and widths of 50–500.

A. Magnetic semiconductor with canted antiferromagnetism

The behavior of $Eu_5Sn_2As_6$ can be classified as that of a narrow-gap-canted antiferromagnetic semiconductor. Upon cooling, $Eu_5Sn_2As_6$ acts similarly to an ordinary narrow gap semiconductor [9], as evidenced in Fig. 1(c). Hall effect measurements at 300 K—well above the onset of magnetic fluctuations—give a hole-carrier density of $1.75 \times 10^{18}\ cm^{-3}$,

[*]These authors contributed equally to this work.
[†]Contact author: analytis@berkeley.edu

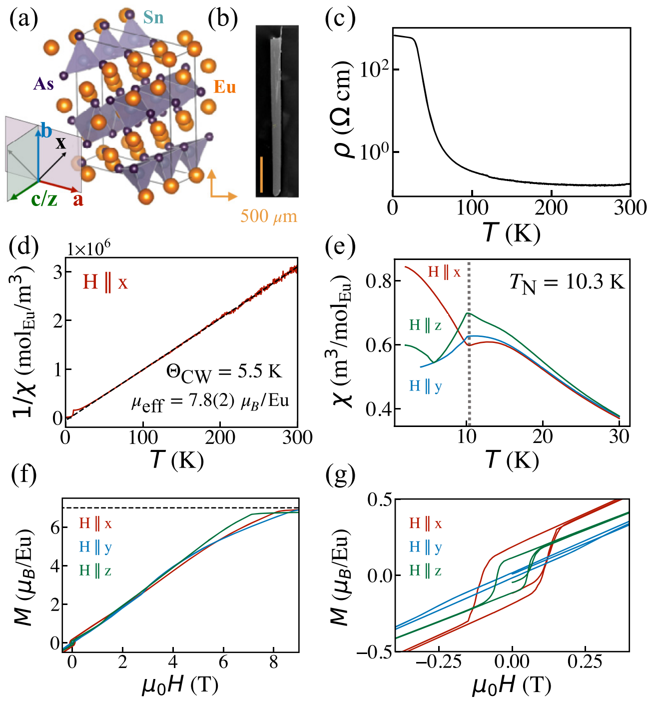

FIG. 1. (a) Crystal structure of $Eu_5Sn_2As_6$, with the coordinate frame as used throughout the text. (b) SEM micrograph of a crystal with the long axis along the Sn-As chains. (c) Zero-field resistivity ρ_{zz} plotted as a function of temperature. (d) Field-cooled inverse magnetic susceptibility χ_{zz}^{-1}, with an applied field of 20 mT. The dashed black line shows a Curie-Weiss fit as described in the main text. (e) Low-temperature field-cooled magnetic susceptibility χ_{ii} for different field directions. Applied field is 20 mT in all cases, with $i = x, y$, and z given by the red, blue, and green curves, respectively. (f) Isothermal field sweeps for the three orthogonal field directions at 2 K, with the dotted line at 7 μ_B/Eu (expected saturation moment of a free Eu^{2+} ion). (g) Enlargement of the low-field region of the same isothermal field sweeps.

indicating a very low concentration of carriers. The low-field Hall coefficient grows precipitously as the temperature is lowered, as the carrier density drops with a functional form typical of thermally activated carriers. This low carrier density in $Eu_5Sn_2As_6$ contrasts with the majority of other Eu-based magnetic topological-insulator candidate materials, wherein the bulk carrier density is an order of magnitude larger [10–12]. This highlights why the study of this family of materials as magnetic topological insulators is needed.

In addition to the Hall result, the low-temperature resistance is well fit by a simple activated Arrhenius function with a gap of 35 meV, as plotted in Appendix Fig. 6. Below $T \sim 25$ K however, the resistance increases further only polynomially resulting in a "knee" in the data, as shown in Fig. 1(c). We note that the precise temperature of this feature, as well as the level of saturation, is somewhat variable between samples. We discuss the possible origins of this saturation in Sec. III.

From a Curie-Weiss fit to the high-temperature magnetic susceptibility—plotted in Fig. 1(d)—the fluctuating moment is $\mu_{\rm eff} = 7.8(2)\mu_{\rm B}$/Eu, indicating that Eu is in a 2+ valence, with a $J = S = 7/2$ configuration. To within the experimental mass uncertainty of the crystal, this is in excellent agreement with the expectation of $7.93\mu_{\rm B}$ for isolated Eu^{2+} moments.

The same Curie-Weiss fit gives a positive $\Theta_{\rm CW} = 5.5$ K—typically an indicator of a ferromagnetic ground state. Indeed, a previous characterization of the material [4] reported $Eu_5Sn_2As_6$ to be a ferromagnet. However, as shown in Fig. 1(e), we observe a suppression of the moment below $T_{\rm N} = 10.3$ K when the field is along either of the y or z directions, which instead implies antiferromagnetic behavior. A second transition is also observed at $T_{\rm N'} = 9.4$ K, below which a small hysteresis loop opens in the field-dependent magnetization for fields along x or z but not along y [Figs. 1(f) and 1(g)]. The hysteresis loop corresponds to a static moment of approximately $0.2\mu_{\rm B}$ per Eu ion at 2 K for all field projections away from $H \parallel y$. This suggests that $Eu_5Sn_2As_6$ is an antiferromagnet with canted moments in the x and z directions. Such a strong angular anisotropy is somewhat surprising on account of the modest orthorhombicity of the material, but is corroborated by the angle-dependent magnetoresistance, shown in Appendix Fig. 10.

B. Interacting orders, metamagnetic transitions, and anisotropic spin dynamics

In $Eu_5Sn_2As_6$, Eu occupies three symmetry inequivalent sites (Appendix Fig. 5), and a comparison of bond lengths indicates that, even when considering just direct exchange between neighboring Eu-sites, there are at least five relevant exchange pathways. Incorporating indirect-exchange mediated by the SnAs chains, or second-order Eu-Eu exchange at greater distances, only compounds this complexity. Therefore, in the absence of direct probes of the magnetic structure, we can only infer the nature of these ordered states from the hierarchy of competing interactions in the material and the cross-referencing of various bulk probes.

As shown in Figs. 2(a) and 2(b), upon increasing temperature from 2 K the saturation moment and coercive field of the field hysteresis both evolve in a nonmonotonic fashion. Specifically, the hysteresis collapses around 7.4 K, before reemerging and then disappearing again above $T_{\rm N}$. The coercive field instead diverges at the collapse, and exhibits an approximately saturated value at the lowest temperatures. This gives an indication that the orders which set in at $T_{\rm N} = 10.3$ K (AFM-1) and $T_{\rm N'} = 9.4$ K (cAFM) are, in fact, coexisting and interacting, such that the static moment evolving below 7.4 K is distinct from that of the original ordering at $T_{\rm N}$. The collapse of the saturated moment at 7.4 K is, therefore, not a phase transition, but a manifestation of the coexistence of the two interacting orders. This is corroborated by the zero-field heat capacity (Appendix Fig. 8), which shows only two peaks at $T_{\rm N}$ and at $T_{\rm N'}$.

We further observe exchange bias in the minor hysteresis loops, plotted in Fig. 2(c) for field oriented along z. While exchange bias phenomena are most familiar in the context of AFM-FM heterostructures [13], similar physics is found in various systems with interacting or competing order parameters [14]. The presence of exchange bias suggests that cAFM and AFM-1 phases coexist and interact, where the latter pin the canted moments of cAFM. In such a picture, the ordered

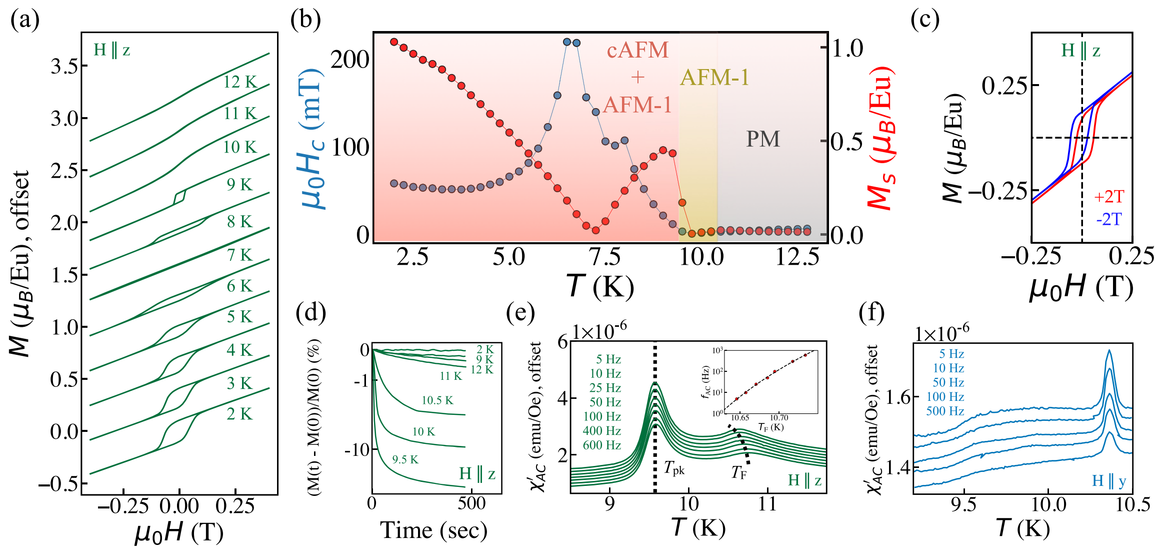

FIG. 2. (a) Low-field field sweeps for $H \parallel z$ at temperatures 2–12 K, to show the evolution of the hysteresis loops with temperature (offset for clarity). (b) Saturation moment (red) and coercive field (blue) of the hysteresis loops as a function of temperature, with the paramagnetic (PM), AFM-1, and canted AFM + AFM-1 phases labeled. (c) Low-field magnetization as a function of field at 2 K, with field oriented along z. The red/blue curves show data taken following field cooling in ± 2 T from outside the ordered state. (d) Isothermal relaxation curves at a range of temperatures. See main text for the sequence of measurement. (e, f) AC magnetic susceptibility with decreasing temperature for a range of different frequencies, for fields $H \parallel z$ and $H \parallel y$, respectively, and a driving field of 0.3 mT. The inset in (e) shows the frequency-dependent shift of the transition temperature T_F and its corresponding Vogel-Fulcher fit, as described in the main text.

states would have to originate at distinct, exchange coupled magnetic sites.

This coexistence also likely leads to frustration in the magnetic lattice, which manifests as glassy dynamics in the magnetization relaxation, Fig. 2(d). For each data set, the sample has been cooled from 50 K to the specified final temperature in a 0.1 T field, then after allowing the sample to thermalize for 5 minutes, the field is turned off and the magnetization is recorded as a function of time. For an ordered system with a static moment, one expects the magnetization to endure indefinitely. Conversely, the magnetization of a paramagnetic system should rapidly follow the field to zero. The observation of slow dynamics in the narrow window $T_{N'} < T < T_N$ suggests a strong frustration from the interplay between the two order parameters. This also distinguishes this behavior from glassy dynamics resulting from quenched disorder, which should manifest down to the lowest temperatures.

To further examine the interplay of order parameter competition and quenched disorder we have employed AC magnetic susceptibility (ACMS) measurements. For fields oriented along z, shown in Fig. 2(e), two peaks T_{pk} and T_F are clearly resolved, near to the same temperatures where sharp peaks are observed in the heat capacity measurements (Appendix Fig. 8). The ability for ACMS to distinguish closely spaced transitions can be contrasted against the modest kink observed for this orientation in DC magnetic susceptibility. However, as we increase the frequency of the 0.3 mT AC drive field, the higher-temperature transition is observed to shift to even higher temperatures—an unexpected response for a transition into long-range order. The extracted peak temperature T_F—plotted in the inset of Fig. 2(e) for each drive frequency f_{AC}—fits well to the Vogel-Fulcher law

$$f_{AC} \propto \exp\left[-E_a/(T_F - T_0)\right], \tag{1}$$

where E_a is an activation energy and T_0 the characteristic temperature. This has been successfully deployed in describing the observed transitions in canonical spin glasses like Cu_xMn and $Eu_{1-x}Sr_xS$ [15,16]. The extracted T_0 is the asymptotic DC limit of the glass transition, fitted here to $T_0 = 10.3 \pm 0.1$ K. This matches exceptionally well to the location of the zero-field peak in the heat capacity, identified previously as $T_N = 10.3$ K.

T_0 is often interpreted as relating to an incipient long-range order which is destabilized in a glass phase [17]. The agreement between the heat capacity peak at T_N and T_0 is, therefore, surprising, given that canonical spin glasses do not show a sharp peak in heat capacity at their freezing temperatures, but rather a broad hump above T_0. This suggests that the application of a very modest oscillatory field along z perturbs the system away from a long-range ordered phase AFM-1 at T_N and towards what could be a cluster-glass, allowing cAFM to exist undisturbed. This may account for the slight enhancement of T_{pk} as compared to $T_{N'}$.

The influence of the oscillating field is made even more apparent when we rotate its direction. In Fig. 2(f), we demonstrate the effect of applying the AC drive field along $H \parallel y$. For an AC field oriented away from the z-axis, a sharp frequency-independent peak is manifest at 10.3 K, consistent with the heat capacity results. This striking direction dependence in the presence of a small perturbative field ($\mu_0 H_{AC} = 0.3$ mT) suggests that the competition between long-range order and the cluster-glass phase is incredibly tight. While long-range order appears to win out at low temperature in all cases, there

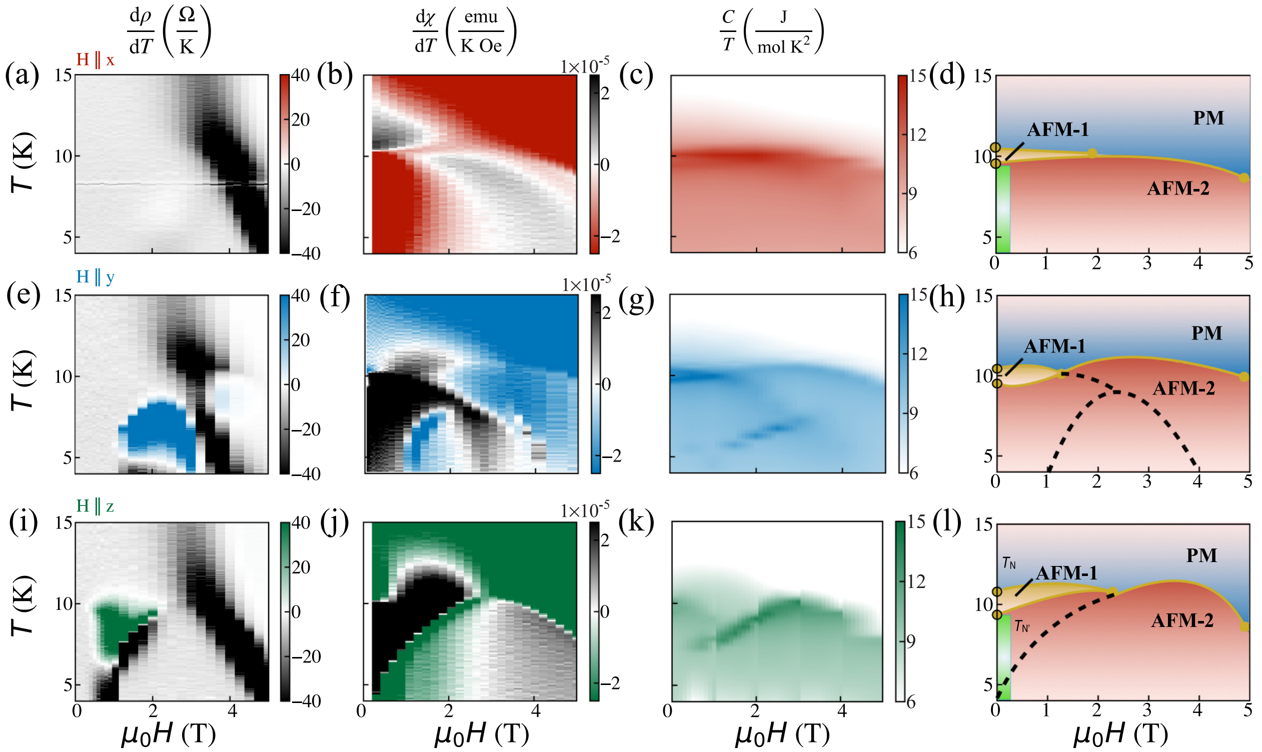

FIG. 3. Contour plots showing the temperature and field variation of (a), (e), and (i) the temperature derivative of the electrical resistivity $d\rho_{zz}/dT$, (b), (f), and (j) the temperature derivative of the magnetic susceptibility $d\chi_{ii}/dT$, and (c), (g), and (k) the heat capacity C/T, for applied fields along the (x, y, z) directions. All data were collected via temperature ramps at a constant field. (d), (h), and (l) show the inferred magnetic phases for the three field directions, as discussed in the main text. Yellow solid lines are guides to the eye to indicate phase transitions, black dotted lines are instead to indicate metamagnetic transitions. The low-field region in green is to mark the cAFM + AFM-1 phase.

remains close competition near the transition temperature, resulting in this very unusual, anisotropic behavior.

Anisotropy also appears in the cascade of apparent phase transitions that are observed below T_N. Save for the outermost phase boundary which separates the ordered phase from the paramagnetic state, the intervening phases depend acutely on the orientation of the field. This observation is carried across all bulk probes of the material surveyed, including resistivity, magnetic susceptibility and heat capacity, as illustrated by the contour plots in Fig. 3. Signatures of this anisotropy also appear in the continuous angle-dependent magnetoresistance curves, plotted in Appendix Fig. 10. The ubiquity of certain features across distinct physical probes—in addition to sharp peaks in the magnetic heat capacity—allows for the identification of bulk phase transitions, which we label with yellow lines in the schematic phase diagrams of Fig. 3. Cases where $d\chi_{ii}/dT$ changes sign but there is no evidence for a sharp heat capacity anomaly we instead attribute to metamagnetic phase transitions, and indicate these with black dotted lines. At higher fields we speculate that the in-field magnetic order is quite similar, and we denote it AFM-2. Given the similarity of the AFM-2 phase boundary in all cases, it seems reasonable that this is a common ground state for all field directions. Notably, this phase is field induced and born from the state where AFM-1 and cAFM coexist. Again, without direct probes of the magnetic structure it is difficult to say anything exact, but given the complexity of the Eu-Eu exchange we do not expect AFM-1 no cAFM to be simple FM or AFM. Rather, it is likely that each is a noncollinear order, which is consistent with the strongly anisotropic magnetic phase diagram which manifests FM and AFM properties in different directions.

C. Interplay of frustration and colossal magnetoresistance

The effects of frustration-driven glassy dynamics appear not to be restricted to the temperature interval directly above cAFM, but instead manifest at much higher temperatures, impacting the observed transport and thermodynamic properties. This can be inferred from the magnetic heat capacity, which is isolated by subtracting a phonon background (see Appendix D). We define

$$S_{\mathrm{mag}}(T) = \int_{T_{\mathrm{min}}}^{T} dT' \frac{C_{\mathrm{mag}}(T')}{T'}, \tag{2}$$

where $T_{\mathrm{min}} = 0.35$ K is the base temperature of the measurement. In the limit that the $J = 7/2$ moments arising from Eu^{2+} ions are purely independent (i.e., $k_B T \gg J_{ij}$), the magnetic entropy $S_{\mathrm{mag}} = R\ln(8)$. In Fig. 4(a), the computed zero-field magnetic entropy is plotted as a function of temperature. Rather than jumping to $R\ln(8)$ at T_N as one may expect in moving from a purely paramagnetic to canted-AFM state, the full magnetic entropy is recovered only very slowly, with the transitions manifesting simply as a modest change in slope. Only at temperatures ∼50 K is the anticipated full magnetic entropy recovered, indicating that some degree of local correlations between Eu moments persists far above the ordering temperature.

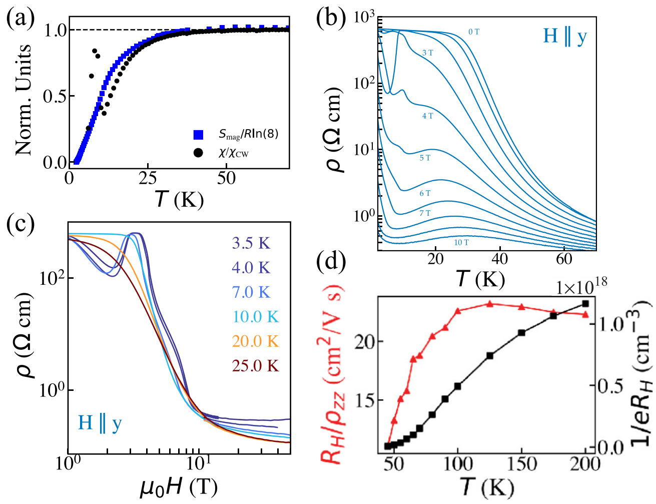

FIG. 4. (a) Magnetic entropy as a fraction of the anticipated total entropy and magnetic susceptibility normalized to the Curie-Weiss law fit at higher temperature [Fig. 1(d)], both plot as a function of temperature. (b) Resistivity as a function of temperature for $H \parallel y$ at constant fields between 0–10 T. (c) Resistivity as a function of field for $H \parallel y$ at constant temperatures between 3.5–25 K. (d) Hall coefficient divided by zero-field resistivity (left) and inverse Hall coefficient (right) plotted as a function of temperature, as extracted from fits to the slope of the Hall voltage V_{xz} in the low field limit ($\mu_0 H < 1$ T), see Appendix Fig. 7.

This interpretation is corroborated by the magnetic susceptibility and angle-dependent magnetoresistance (AMR). For the first, the inverse susceptibility diverges from a high-temperature Curie-Weiss fit—which describes independent moments—at approximately the same temperature (~50 K) as the magnetic entropy begins to reduce from $R\ln(8)$ [shown in Fig. 4(a)]. In the AMR (Appendix Fig. 10), the strong anisotropy observed within the ordered phase persists to at least 60 K. Both measurements, therefore, lend further support to the onset of short-range correlations well above T_{N1}.

The presence of correlations without magnetic order appears to run counter to the conventional estimation of the exchange frustration parameter $f = T_N/T_{CW} = 10.3/5.5 = 1.87 > 1$, suggesting a lack of frustration. However, it is essential to note that the simple frustration parameter f is an appropriate proxy for frustration when a single exchange parameter is dominant [18]. Only in this limit is there a straightforward correspondence between J_{ij} and T_{CW}, the second of which should be thought of more as a weighted sum over all exchange terms in the system. Given the rather complex exchange network illustrated in Appendix Fig. 5, the long tail of the magnetic entropy is a more suitable metric for frustration in the present system.

The onset of correlations also coincides with the onset of colossal magnetoresistance (CMR). As plotted in Figs. 4(b) and 4(c), the magnetoresistance becomes significant at lower temperatures. At 50 K, a field of $\mu_0 H = 10$ T results in an order of magnitude reduction in the resistivity $\rho_{zz}(T)$. By 25 K, the same field leads to a drop in resistivity of 600 000%. As evidenced by the high field data in Fig. 4(c), the magnitude of the CMR asymptotically converges towards this low resistance state by $\mu_0 H = 10$ T and the material does not become metallic out to the largest fields measured. This suggests that the mechanism for the observed CMR is associated with spin-scattering mechanisms, likely spins associated with the correlated Eu^{2+} moments, as opposed to a field-driven closure of the band gap. This is consistent with the 35 meV band gap estimated from Arrhenius fitting of electric transport (Appendix B), which would require a field of 7800 T to close.

Hall effect data further demonstrates the interplay between magnetic correlations and the charge carriers in $Eu_5Sn_2As_6$, as shown in Fig. 4(d) (and Appendix C). The carrier density is consistent with thermally activated carriers, and appears to decay asymptotically towards zero at low temperature. This contrasts with the carrier mobility—which we infer from the ratio of the zero-field Hall coefficient to the longitudinal resistivity—which instead remains approximately constant down to 100 K, before a sharp decline at lower temperatures. This collapse can be attributed to scattering of carriers from magnetic clusters which continue to grow as temperature is reduced. The scattering of dilute carriers by magnetically ordered clusters has been seen previously in this class of compounds through the formation of magnetic polarons, which supersede the role of free carriers in the system. As clusters continue to grow, propagation of a carrier through the disordered magnetic landscape requires a series of spin-flip events, resulting here in an enhanced effective mass and declining mobility.

III. DISCUSSION

Magnetic polarons have previously been seen in a variety of narrow-gap semiconductors such as the manganites [19,20], and other Eu-based compounds such as EuB_6 [21]. Of particular relevance is $Eu_5In_2Sb_6$ which possesses the same structure as $Eu_5Sn_2As_6$ and has recently been reported [2,22–25] to host magnetic polarons. In this system, magnetic polarons have been shown to increase in size as temperature is lowered below 200 K while the resistivity rises and ultimately develops into CMR. While this picture is consistent with our data on $Eu_5Sn_2As_6$, further measurements are required to prove the role of magnetic polarons are the same as suggested by studies in $Eu_5In_2Sb_6$. Preliminary microwave impedance microscopy measurements indicate an inhomogeneously conductive surface with spatially localized regions of high resistivity, shown in Appendix Fig. 11. However, a connection between these spatially localized regions and the bulk conductivity requires further study.

The richness of the magnetic phase diagram of $Eu_5Sn_2As_6$, shown in Fig. 3, reflects the underlying complexity of the exchange interactions, and it is reasonable that this might be the cause of the CMR. The picture of current carrying magnetic polarons is consistent with our observations and already discussed for the related system $Eu_5In_2Sb_6$ [2,22,24]. Here the dressed quasiparticles are increasingly localised by the growing influence of the exchange interactions, a process that is rapidly suppressed by the application of magnetic fields. However, we note that other models might also explain the CMR observed here. For example, recent studies of noncollinear magnets thought to host loop currents, like $Mn_3Si_2Te_6$ [26], show very similar CMR to that reported here. Further studies are required to distinguish these possibilities.

While the CMR reported here is exceptionally large, we believe that it is, in fact, only an approximate lower bound on the bulk magnetoresistance in this material, as the low-temperature, zero-field resistivity appears to shunt across a low-resistance path. This manifests as a kink or knee in ρ_{ii}(T) below approximately 30 K and limits our ability to evaluate the absolute scale of negative CMR in this system. Notably, this is different to $Eu_5In_2Sb_6$, where the resistivity is strongly suppressed below the magnetic transition but then continues to grow without saturating to the lowest measured temperature [2].

Surface states would provide a plausible explanation for this shunting, as their comparatively small current capacity would limit our ability to identify their contribution at high temperatures where the large cross section of the samples ($\sim$0.04 mm^2) would dominate the transport. This is similarly true for the low-temperature magnetoresistance as the bulk CMR pulls ρ_{zz} below the shunt value (for this sample $\rho_{zz} < 70$). Moreover, the absence of any associated features in the susceptibility and heat capacity in these same regions of phase space severely limits the volume fraction that might contribute to any sort of bulk transition.

A surface state contribution to the resistivity in $Eu_5Sn_2As_6$ is reasonable. Topologically trivial surface states in narrow gap semiconductors were investigated in narrow gap semiconductors such as InSb and (Hg,Cd)Te [9]. In this case, dangling bond states caused by surface termination in semiconductors induce band bending at the surface and result in a surface accumulation layer of carriers. Topological surface states may also contribute as predicted in DFT calculations for materials in the $Eu_5M_2X_6$ family [2,3]. However, these calculations assume an A-Type AFM magnetic order, whereas the properties of $Eu_5Sn_2As_6$ measured in this study point toward a magnetic structure that is far more complex. To date, no experimental evidence has been found that these materials are indeed topological. However, this would be the first material in this family to evidence surface states of any kind, suggesting the merits of further study.

IV. CONCLUSION

Magnetic Zintl semiconductors offer a wealth of opportunities for the development and study of new phenomena through their combination of narrow gaps and geometric confinement. We presented a comprehensive characterization of the magnetic and electronic properties of $Eu_5Sn_2As_6$ across its entire low-temperature phase diagram. The presence of multiple symmetry-distinct Eu sites per unit cell, combined with the exchange-frustrated network of magnetic interactions in the system provide the requisite conditions to support a complex magnetic phase diagram, which itself shows a very tight competition with cluster-glass dynamics upon application of even very modest applied fields. This tension between long-range order and glass physics manifests in all experimental probes surveyed, including magnetization, heat capacity, and magnetoelectrical transport. We observe the effects of competing orders and interactions for temperatures almost an order of magnitude greater than T_N, a fact which is surprising given the absence of sufficient carriers to mediate exchange via for example the Ruderman–Kittel–Kasuya–Yosida (RKKY) mechanism. Most notably, the interaction between the dilute thermally activated carriers in the system and the local moments give rise to colossal magnetoresistance of at least 600 000%, likely through the formation of magnetic polarons via scattering of carriers off of magnetic clusters. At the lowest temperatures measured, the bulk conductivity is shunted by another conduction channel, which could originate from surface states. Future experiments will be required to elucidate the true nature of the various metamagnetic orders in the system as well as the nature of the shunting of the electrical resistivity at low temperature, and may reveal a connection to a nontrivial topology in this system.

ACKNOWLEDGMENTS

This research was supported by he Air Force Office of Scientific Research (AFOSR) Multidisciplinary University Research Initiative (MURI) grant on TOPological Flat bands fOr Correlated Electron systems (TOPFORCE) under the Award No. FA9550-22-1-0270. R.P.D. was supported by the Canadian Government under a Banting Fellowship. Work at the National High Magnetic Field Laboratory was supported by NSF Cooperative Agreements No. DMR-1644779 and No. DMR-2128556, the U.S. Department of Energy (DOE), and the State of Florida. J.S. acknowledges support from the DOE Basic Energy Sciences FWP “Science of 100 T.”

APPENDIX A: EU-EU EXCHANGE PATHWAYS

The unit cell of $Eu_5Sn_2As_6$ is complex, with three separate Europium Wyckoff positions and a number of closely spaced nearest neighbor Eu-Eu distances even within the *x*-*y* plane, shown in Fig. 5. This implies a competition between Heisenberg exchange pathways and allows for a variety of types of magnetic order within this material.

APPENDIX B: ARRHENIUS MODEL FIT OF ELECTRIC RESISTIVITY

Figure 6(a) shows an Arrhenius plot of the electrical resistivity as a function of inverse temperature, where a straight line implies that the data follows the Arrhenius model of

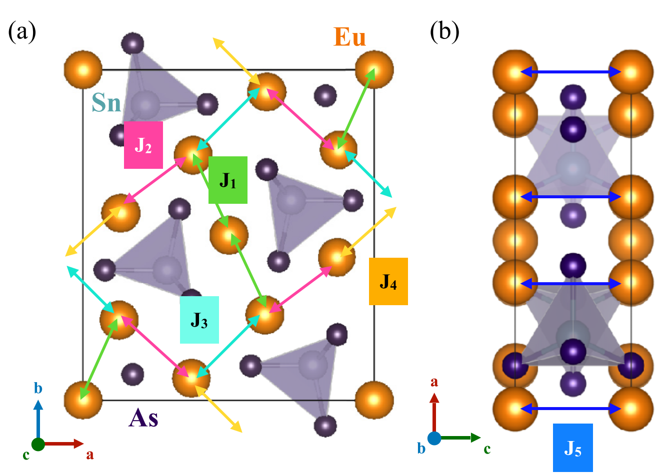

FIG. 5. The unit cell of $Eu_5Sn_2As_6$ viewed along (a) the *c*-axis, and (b) the *b*-axis, including a schematic illustration of the nearest-neighbor exchange pathways between inequivalent Eu moments.

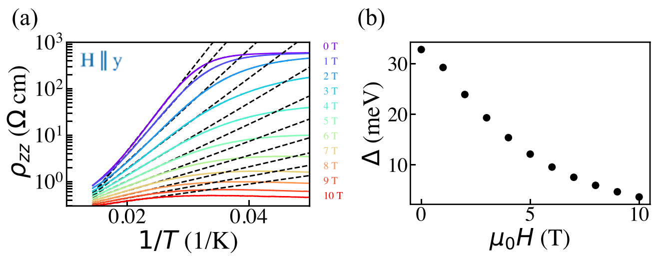

FIG. 6. (a) Electrical resitivity of $Eu_5Sn_2As_6$ at different fields from 0 T to 10 T plotted on a log-log scale against inverse temperature for $H \parallel y$. (b) Evolution of the fitted gap Δ as a function of applied field.

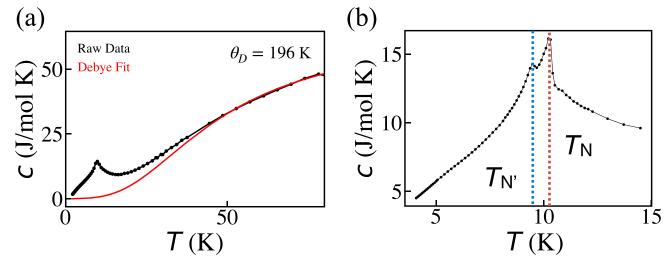

FIG. 8. (a) Zero-field heat capacity plotted as a function of temperature, where the solid line shows the Debye fit. (b) The magnetic heat capacity, with the estimated phonon contribution having been subtracted.

thermally activated carriers, $\rho \sim \exp(\Delta/k_B T)$. This is indeed the case for the intermediate temperature data in all measured fields, and the fitted gap Δ is plotted as a function of applied field in Fig. 6(b). The zero-field value is 35 meV, and decreases with increasing field.

APPENDIX C: HALL RESISTIVITY

The magnetoresistance and Hall transport can be used to assess the evolution of the carrier concentration and mobility with temperature and can shed light on the impact of magnetic correlations at lower temperature. The simplest approach to modeling a narrow gap semiconductor is with a two carrier model where the carrier's mobility and density are taken to be independent of field. In this simple picture, the resistivity ρ scales as positive B^2. However, the magnetoresistance of $Eu_5Sn_2As_6$ has a negative B^2 dependence, making any multicarrier model with a field-independent mobility and carrier density impossible to fit. This implies that the carrier mobility or density evolves as a function of field and cannot be disentangled from electric transport alone. This makes it difficult to quantitatively assess the effect of temperature on the carrier's mobility and, instead, we track the zero-field Hall coefficient as well as its ratio to the longitudinal resistivity as a function of temperature, plotted in Fig. 4(d), with fits made to the data shown in Fig. 7.

Low-field Hall effect measurements below ∼50 K are difficult due to the longitudinal resistivity being orders of magnitude larger than the transverse resistivity, and thus dominating the Hall voltage signal in the presence of any misalignment in the Hall contacts. As a result, even after antisymmetrizing with respect to field, below ∼40 K the signal-to-noise ratio determined by our lock-in setup is insufficient to detect the Hall voltage.

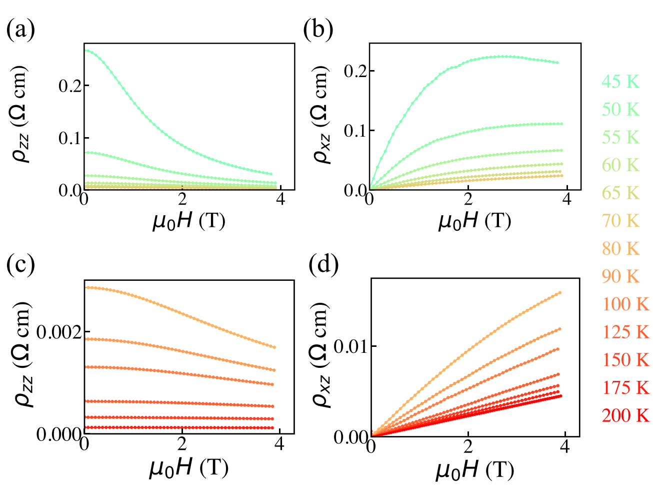

FIG. 7. (a), (c) Longitudinal resistivity ρ_{zz} plotted as a function of applied field $H \parallel y$ at a range of constant temperatures between 45–200 K. (b), (d) Hall resistivity ρ_{xz} under the same conditions.

APPENDIX D: MAGNETIC HEAT CAPACITY

The total heat capacity is the sum of contributions from the electronic, vibrational (phononic), and magnetic degrees

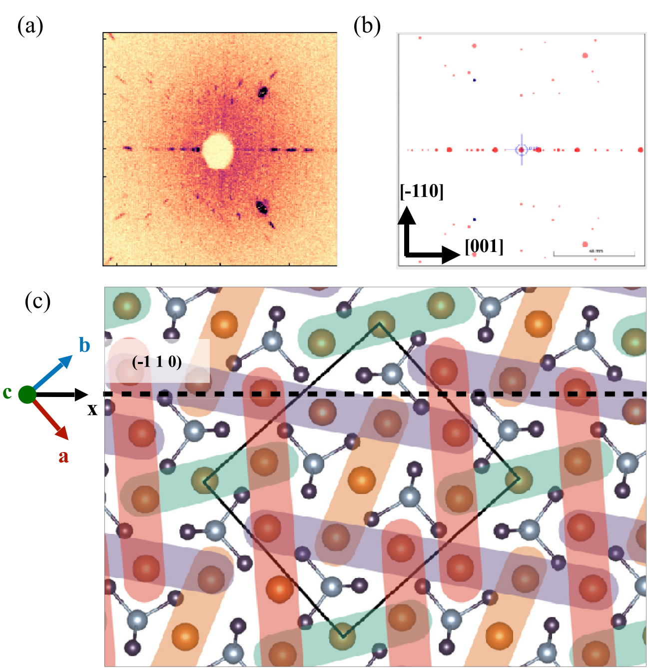

FIG. 9. (a) Laue diffraction of $Eu_5Sn_2As_6$. (b) The QLaue fit from the $Eu_5Sn_2As_6$ cif file. (c) Schematic of the $Eu_5Sn_2As_6$ crystal structure, with the unit cell shown by the solid lines and the natural crystal termination along the (-110) plane by the dotted line. Also included are shaded regions to emphasize plaquettes of the closest-spaced Eu sites.

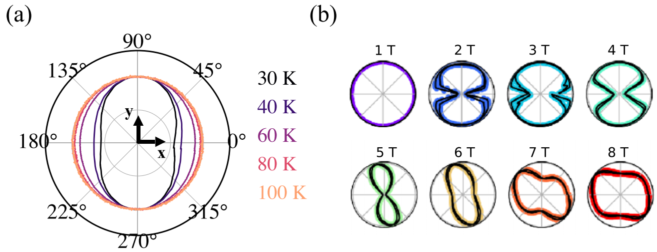

FIG. 10. AMR in the a-b plane, with 0° parallel to x. (a) Plotted at various constant temperatures, with an applied field of 2 T. (b) Plotted at various constant fields, at a temperature of 5 K.

of freedom

$$C(T) = C_{\mathrm{el}}(T) + C_{\mathrm{ph}}(T) + C_{\mathrm{mag}}(T). \tag{D1}$$

To isolate the magnetic heat capacity it is, therefore, necessary to subtract the electron and phonon contributions. For a semiconductor with bandgap of 35 meV (~400 K), the electron contribution will be negligible at the temperatures under consideration. For the latter, in the absence of a nonmagnetic analog compound we assume that the phonon contribution will follow a Debye law

$$C_{\mathrm{ph}}(T) = 9R\left(\frac{T}{\Theta_D}\right)^3 \int_0^{\Theta_D/T} x^4 \frac{e^x}{(e^x - 1)^2}\, \mathrm{d}x, \tag{D2}$$

where R is the gas constant and Θ_D the Debye temperature. Given the magnetic interaction energy scales, we expect the phonon contribution to dominate at high temperatures, and therefore, fit the heat capacity data between 60–80 K to the Debye model to give $\Theta_D = 196$ K [shown in Fig. 8(a)]. Subtraction of this contribution then gives the magnetic heat capacity, a portion of which is shown in Fig. 8(b). As described in the main text, this can be used to obtain the magnetic entropy [Fig. 4(a)].

APPENDIX E: ANISOTROPY FROM STRUCTURE AND AMR

$Eu_5Sn_2As_6$ crystals grow as prisms with a cross-section that has one large crystal facet. As shown in Fig. 1, we define the longest side of the needle-like crystals to be the z-direction and the largest crystal facet to be perpendicular to the y-direction. Laue diffraction analysis using the software program QLaue then shows that the x-direction is parallel to (−110), cutting the unit cell as seen in Appendix Fig. 9(c).

Angular magnetoresistance (AMR) measurements were performed using the standard four-terminal electric transport configuration, with the applied current along the z-direction and the rotation in the a-b plane (equivalently x-y plane), with 0° defined parallel to the x-axis. Figure 10(a) shows the AMR at different temperatures, and indicates a breaking of U(1) symmetry in the a-b plane below 80 K, perhaps in conjunction with the formation of magnetic polarons. Figure 10(b) shows the AMR at 5 K at a range of fields, where the positions of the extrema evolve with field. The 90° rotation of the extrema at high fields is concurrent with the AFM-2 phase boundary

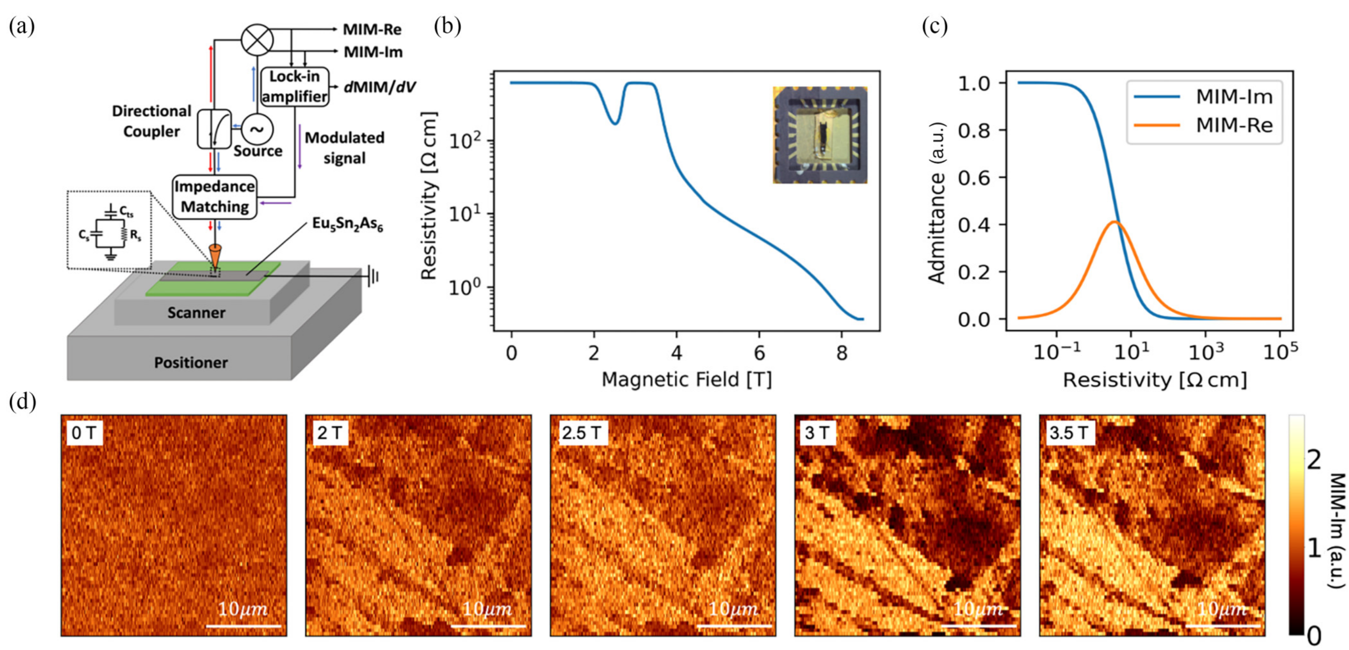

FIG. 11. Spatially resolved conductivity profile of $Eu_5Sn_2As_6$ obtained using microwave impedance microscopy (MIM). (a) Schematic illustration of the MIM measurement setup, where the tip-sample interaction with the sample is abstracted using a lumped-element model. (b) Two-terminal transport measurement conducted in as a function of out-of-plane magnetic field ($H \parallel y$) and at $T = 4$ K. Inset: Optical image of the $Eu_5Sn_2As_6$ crystals crystal. (c) Theoretical MIM response curves, simulated using finite element analysis at 3 GHz, show how the reflected microwave signal depends on the local resistivity of the sample. The real and imaginary parts of the reflected signal are denoted MIM-Re (red) and MIM-Im (blue), respectively. (d) Spatially resolved MIM images obtained in at a series of increasing magnetic fields, applied out-of-plane. MIM-Im, the imaginary part of the microwave response, is plotted in each image. The MIM measurement frequency is 3 GHz, and the temperature is 100 mK. Each scale bar is 10 μm.

(Fig. 3), suggesting that the anisotropy in the AMR is linked to the bulk magnetic order.

APPENDIX F: MICROWAVE IMPEDANCE MICROSCOPY

We performed microwave impedance microscopy (MIM) measurements to image the evolution of the real-space conductivity profile as a function of the out-of-plane magnetic field ($H \parallel y$) at low temperatures ($T = 100$ mK). As illustrated in Fig. 11, we observed microscopic spatial variations in the amplitude of the reflected MIM signal, which suggests an inhomogeneous conductivity landscape with circular pockets of high resistivity (dark clusters) that coexist with large-area conductive domains (bright rectangular regions). Further imaging work would be required to investigate the percolation of magnetic polarons in detail.

[1] C. Haas, Magnetic semiconductors, C R C Critical Reviews in Solid State Sciences **1**, 47 (1970).

[2] P. Rosa, Y. Xu, M. Rahn, J. Souza, S. Kushwaha, L. Veiga, A. Bombardi, S. Thomas, M. Janoschek, E. Bauer, M. Chan, Z. Wang, J. Thompson, N. Harrison, P. Pagliuso, A. Bernevig, and F. Ronning, Colossal magnetoresistance in a nonsymmorphic antiferromagnetic insulator, npj Quantum Mater. **5**, 52 (2020).

[3] N. Varnava, T. Berry, T. M. McQueen, and D. Vanderbilt, Engineering magnetic topological insulators in $Eu_5M_2X_6$ Zintl compounds, Phys. Rev. B **105**, 235128 (2022).

[4] J. Wang, S.-Q. Xia, and X.-T. Tao, $A_5Sn_2As_6$ (A = Sr, Eu). Synthesis, crystal and electronic structure, and thermoelectric properties, Inorg. Chem. **51**, 5771 (2012).

[5] A. B. Childs, S. Baranets, and S. Bobev, Five new ternary indium-arsenides discovered. Synthesis and structural characterization of the Zintl phases $Sr_3In_2As_4$, $Ba_3In_2As_4$, $Eu_3In_2As_4$, $Sr_5In_2As_6$ and $Eu_5In_2As_6$, J. Solid State Chem. **278**, 120889 (2019).

[6] A. M. Goforth, P. Klavins, J. C. Fettinger, and S. M. Kauzlarich, Magnetic properties and negative colossal magnetoresistance of the rare earth Zintl phase $EuIn_2As_2$, Inorg. Chem. **47**, 11048 (2008).

[7] Z. Ren, Q. Tao, S. Jiang, C. Feng, C. Wang, J. Dai, G. Cao, and Z. Xu, Superconductivity induced by phosphorus doping and its coexistence with ferromagnetism in $EuFe_2(As_{0.7}P_{0.3})_2$, Phys. Rev. Lett. **102**, 137002 (2009).

[8] K. P. Devlin, B. Gomez, and S. M. Kauzlarich, Thermoelectric properties of p- and n-type $Eu_5Sn_2As_6$, Z. Anorg. Allg. Chem. **648**, e202100386 (2022).

[9] S. M. Sze and M. K. Lee, *Semiconductor Devices, Physics, and Technology*, 3rd ed. (Wiley, Hoboken, NJ, 2012).

[10] T. Sato, Z. Wang, D. Takane, S. Souma, C. Cui, Y. Li, K. Nakayama, T. Kawakami, Y. Kubota, C. Cacho, T. K. Kim, A. Arab, V. N. Strocov, Y. Yao, and T. Takahashi, Signature of band inversion in the antiferromagnetic phase of axion insulator candidate $EuIn_2As_2$, Phys. Rev. Res. **2**, 033342 (2020).

[11] J. Yan, Z. Z. Jiang, R. C. Xiao, W. J. Lu, W. H. Song, X. B. Zhu, X. Luo, Y. P. Sun, and M. Yamashita, Field-induced topological Hall effect in antiferromagnetic axion insulator candidate $EuIn_2As_2$, Phys. Rev. Res. **4**, 013163 (2022).

[12] H. Li, W. Gao, Z. Chen, W. Chu, Y. Nie, S. Ma, Y. Han, M. Wu, T. Li, Q. Niu, W. Ning, X. Zhu, and M. Tian, Magnetic properties of the layered magnetic topological insulator $EuSn_2As_2$, Phys. Rev. B **104**, 054435 (2021).

[13] R. L. Stamps, Mechanisms for exchange bias, J. Phys. D **33**, R247 (2000).

[14] E. Maniv, R. A. Murphy, S. C. Haley, S. Doyle, C. John, A. Maniv, S. K. Ramakrishna, Y.-L. Tang, P. Ercius, R. Ramesh, A. P. Reyes, J. R. Long, and J. G. Analytis, Exchange bias due to coupling between coexisting antiferromagnetic and spin-glass orders, Nat. Phys. **17**, 525 (2021).

[15] J. Tholence, A.C. susceptibility of CuMn and AgMn spin-glasses, Physica B+C **108**, 1287 (1981).

[16] H. Maletta and W. Felsch, Insulating spin-glass system $Eu_xSr_{1-x}S$, Phys. Rev. B **20**, 1245 (1979).

[17] J. A. Mydosh, *Spin Glasses: An Experimental Introduction* (Taylor and Francis, New York, 1993).

[18] A. P. Ramirez, Strongly geometrically frustrated magnets, Annu. Rev. Mater. Sci. **24**, 453 (1994).

[19] R. Kusters, J. Singleton, D. Keen, R. McGreevy, and W. Hayes, Magnetoresistance measurements on the magnetic semiconductor $Nd_{0.5}Pb_{0.5}MnO_3$, Phys. B: Condens. Matter **155**, 362 (1989).

[20] V. Moshnyaga, K. Gehrke, O. I. Lebedev, L. Sudheendra, A. Belenchuk, S. Raabe, O. Shapoval, J. Verbeeck, G. Van Tendeloo, and K. Samwer, Electrical nonlinearity in colossal magnetoresistance manganite films: Relevance of correlated polarons, Phys. Rev. B **79**, 134413 (2009).

[21] P. Das, A. Amyan, J. Brandenburg, J. Müller, P. Xiong, S. von Molnár, and Z. Fisk, Magnetically driven electronic phase separation in the semimetallic ferromagnet EuB_6, Phys. Rev. B **86**, 184425 (2012).

[22] M. V. Crivillero, S. Rößler, P. F. S. Rosa, J. Müller, U. K. Rößler, and S. Wirth, Surface and electronic structure at atomic length scales of the nonsymmorphic antiferromagnet $Eu_5In_2Sb_6$, Phys. Rev. B **106**, 035124 (2022).

[23] S. Ghosh, C. Lane, F. Ronning, E. D. Bauer, J. D. Thompson, J.-X. Zhu, P. F. S. Rosa, and S. M. Thomas, Colossal piezoresistance in narrow-gap $Eu_5In_2Sb_6$, Phys. Rev. B **106**, 045110 (2022).

[24] J. C. Souza, S. M. Thomas, E. D. Bauer, J. D. Thompson, F. Ronning, P. G. Pagliuso, and P. F. S. Rosa, Microscopic probe of magnetic polarons in antiferromagnetic $Eu_5In_2Sb_6$, Phys. Rev. B **105**, 035135 (2022).

[25] V. C. Morano, J. Gaudet, N. Varnava, T. Berry, T. Halloran, C. J. Lygouras, X. Wang, C. M. Hoffman, G. Xu, J. W. Lynn, T. M. McQueen, D. Vanderbilt, and C. L. Broholm, Noncollinear 2k antiferromagnetism in the Zintl semiconductor $Eu_5In_2Sb_6$, Phys. Rev. B **109**, 014432 (2024).

[26] Y. Zhang, Y. Ni, H. Zhao, S. Hakani, F. Ye, L. DeLong, I. Kimchi, and G. Cao, Control of chiral orbital currents in a colossal magnetoresistance material, Nature (London) **611**, 467 (2022).